NANO LETTERS

pubs.acs.org/NanoLett Letter

Photocurrent Saturation Mechanisms in Colloidal Quantum Dot Photodetectors

Korneel Molkens, Yu-Hao Deng, Ezat Kheradmand, Dries Van Thourhout, Zeger Hens,* and Pieter Geiregat*

Cite This: *Nano Lett.* 2026, 26, 8315−8322 Read Online

ACCESS | Metrics & More | Article Recommendations | Supporting Information

ABSTRACT: Colloidal quantum dot photodiodes (QDPDs) are becoming an increasingly mature technology for infrared sensing and imaging that can offer high detectivity, short response times, and micrometer-scale pixelation. Even so, QDPDs suffer from a limited linear dynamic range (LDR), with photocurrents saturating at modest light intensities. Here, we analyze this remaining QDPD bottleneck in PbS-based QDPDs through operando transient absorption spectroscopy. As compared to isolated QDs, we find that recombination of photogenerated charge carriers accelerates in device-ready QD films and full QDPD stacks. Supported by kinetic Monte Carlo simulations, we assign this loss pathway to trion recombination mediated by hopping and doping-induced background charges, and we show that the photocurrent saturates when the rate of trion recombination and charge separation match. On the basis of this result, we argue that the widely varying literature data on the linear dynamic range of QDPDs mainly reflect different carrier extraction rates and conclude that faster carrier extraction is essential to extend the linear dynamic range.

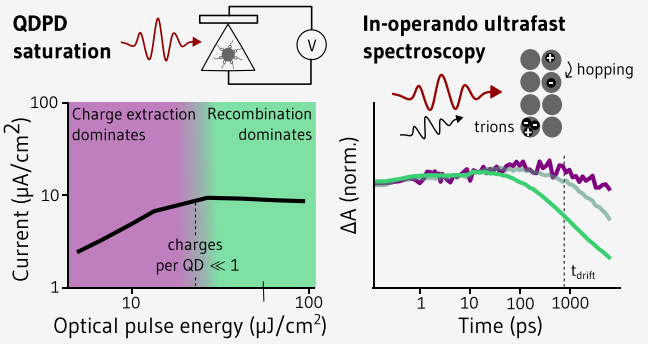

KEYWORDS: *in-operando spectroscopy, ultrafast spectroscopy, photodetectors, nanocrystals, lead sulfide, linear dynamic range*

Photodiodes (PDs) based on thin films of colloidal quantum dots (QDs) show great promise for detection of infrared (IR) light at wavelengths longer than the absorption edge of silicon,[1] a critical spectral range in, for example, time-of-flight applications,[2] machine vision,[3] and chemical sensing.[4] QD-based detectors can be readily integrated with silicon readout circuits to form sensor arrays with micron-size pixels and quantum-efficiency spectra optimized for specific, predefined wavelength ranges. At present, QDPDs using PbS QD are the most mature, a result of optimized synthesis protocols that produce highly monodisperse QDs,[5] and proven methods to form QD thin films with *n*- and *p*-type character.[6,7] PbS QDPDs cover a wavelength range extending from 950 to 2100 nm[8,9] and attain an external quantum efficiency as high as 76%,[10] a detectivity of 2.5×10^{12} Jones at 1300 nm,[8] and a response time as short as 4 ns.[7,11,12] Building on these results, various reports have shown imagers based on PbS QDPD pixel arrays,[13] thereby achieving record-low pixel dimensions of 1.6 μm. Alternative materials to PbS for QD-based IR sensing include HgTe QDs, in particular for sensing of mid infrared light,[14,15] and InAs, InSb, or Ag_2Te QDs for applications where restricted hazardous elements such as Pb and Hg are not accepted.[16−19]

Performance metrics of QDPDs are typically obtained at modest illumination intensities. In the case of PbS QDPDs, for example, photocurrent saturation has been observed with increasing illumination power, with an upper limit of the linear response varying from 5 to 100 and 5000 mW/cm^2.[13,20,21] The limited linear dynamic range (LDR) restricts the application potential of QDPDs since functional sensing requires a linear response. Nevertheless, few studies have addressed this problem,[22] let alone provided an interpretation. Similar to QD devices, isolated QDs show linear responses to low-power illumination, such as photoluminescence or absorption bleaching. In this case, saturation with increasing power is typically ascribed to the formation of short-lived biexcitons within single QDs. This understanding is, however, not directly transferable to QD devices. With a typical absorption cross-section of 10^{-15} cm^2, a saturation power of 5 mW/cm^2 would correspond to an excitation rate per QD of ≈30 s^{-1}. This rate is about 4 orders of magnitude smaller than the recombination rate of single excitons in isolated PbS QDs,[23] which implies that biexcitons rarely form through successive absorption

Received: April 13, 2026
Revised: June 5, 2026
Accepted: June 5, 2026
Published: June 12, 2026

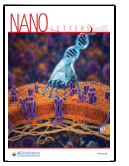

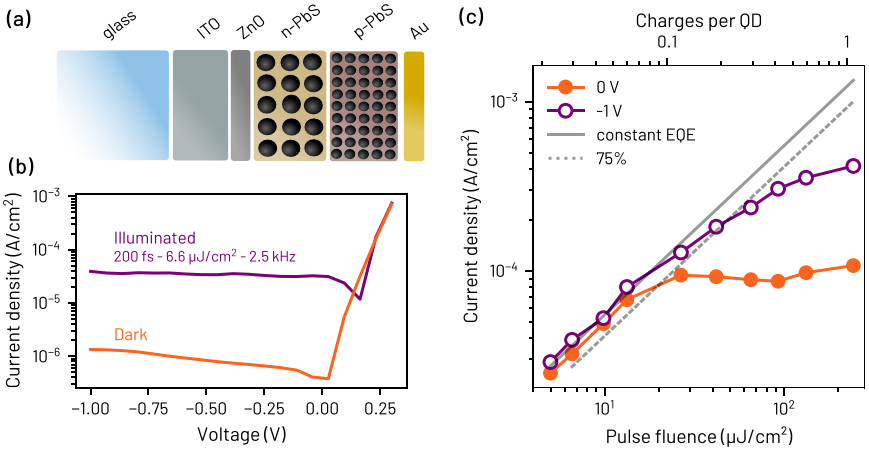

Figure 1. Static characterization of PbS based colloidal quantum dot photodetectors (QDPD). (a) QDPD device architecture used in this work consisting of an ITO bottom electrode, a ZnO QD electron transport (and hole blocking) layer, a small band gap *n*-type PbS QD film (d = 4.6 nm; λ_g = 1300 nm) as an absorbing layer, a larger band gap PbS QD film (d = 3.1 nm; λ_g = 950 nm) as a *p*-type hole transport and electron blocking layer and finally a gold electrode. (b) IV curves of the device with and without illumination by 190 fs pulses at 1200 nm, showing both the low dark current in our QDPDs and the response to pulsed illumination. (c) Current density as a function of pump fluence under pulsed optical excitation. Top horizontal axis indicates the fluence translated to average occupation per QD, $\langle N \rangle$. The gray line indicates a fixed external quantum efficiency. Divergence from this line indicates photocurrent saturation, the origin of limited linear dynamic range (LDR). Reversing bias increases the extracted charge count and therefore pushes the LDR slightly further.

events in single QDs. Saturation occurring at such low occupation levels—well below a single exciton per QD on average—has been assigned to the accumulation of charges on the largest QDs (smallest band gaps) within a film, where Auger recombination causes a rapid loss of trions or biexcitons.[24] However, this mechanism relies heavily on inhomogeneous broadening and seems unlikely given the narrow size distribution of PbS QDs in current state-of-the-art devices.[25]

Here, we address the question of photocurrent saturation in PbS QDPDs through in-operando femtosecond pump−probe spectroscopy. Using a QDPD stack optimized for rapid charge-carrier extraction,[12] we demonstrate that the photocurrent saturates for optical pulses creating $\langle N \rangle \approx 0.1$ excitations per QD. By comparing charge-carrier loss in isolated QDs, device-ready QD films and operating QDPDs, we show that opposite from isolated QDs, device-ready QD films and QDPDs exhibit a recombination pathway that accelerates with increasing charge-carrier density. Supported by kinetic Monte Carlo simulations, we assign this process to trion recombination catalyzed by fast charge hopping in short-ligand films. Importantly, we find that photocurrent saturation occurs when the resulting charge-carrier lifetime matches the ≈1 ns charge-carrier transit time through the QD film. Building on these results, we demonstrate that the charge carrier extraction time is a general predictor of the saturation power for all QDPDs reported in the literature and conclude that QDPDs with a wider linear dynamic range need faster charge carrier extraction architectures.

We used a QDPD device stack in which a photoactive layer of PbS QDs is sandwiched between two charge extraction layers: an electron transport layer consisting of ZnO nanocrystals on ITO-coated glass and a circular gold metal contact with a radius of 0.75 mm; see Figure 1a. As detailed in Supporting Information S1 and previous work,[12] the PbS layer comprised 50 nm of *n*-type PbS QDs with a 1300 nm absorption band-edge—henceforth indicated as PbS-1300 obtained by exchanging the native oleate ligands by tetrabutylammonium iodide (TBAI), and 50 nm of *p*-type PbS QDs with 950 nm absorption band-edge—PbS-950—formed by ligand exchange with ethane-1,2-dithiol (EDT). Shorter ligands facilitate efficient carrier hopping in the QD layers and result in a higher charge carrier mobility, which was previously measured at 10^{-1}−10^{-2} cm²/V for the films used here.[12] Figure 1b shows current density−voltage (J−V) curves of such a device in the dark and illuminated with 1200 nm light from a 190 fs, 2.5 kHz pulsed laser. The resulting time-averaged photocurrent is clearly distinguishable from the dark current of $\approx 10^{-6}$ A/cm². As outlined in Supporting Information S1, the QDPDs have an external quantum efficiency (EQE)—defined as the ratio of the number of extracted electrons and incoming photons per pulse—of 11% at 1200 nm and low excitation fluence. A similar value was obtained under continuous wave (CW) illumination.[12,26] The fall time of the photocurrent after a femtosecond pulse is 1.1 μs, which reflects the RC time constant of the electrical circuit; see Supporting Information S1. Finally, Figure 1c shows the photocurrent as a function of the pump fluence, where deviations from the proportional increase expected for a fixed EQE are clearly visible at a higher fluence. For reasons of consistency (see later), we characterize the onset of photocurrent saturation by the fluence $J_{3/4}$ where the EQE is reduced to 75% of the low-power limit. As outlined in Supporting Information S1, QDPDs from different processing runs yield a voltage-dependent $J_{3/4}$ ranging between 25 and 45 μJ/cm² at −1 V. Using the absorption cross section estimated in Supporting Information S2, the concomitant saturation density of photogenerated charges $\langle N \rangle$ ranges between 0.11 and 0.20 per QD.

For silicon photodiodes, photocurrent saturation was attributed to accelerated charge carrier recombination at a high carrier density.[27] To monitor a similarly density-dependent recombination rate, we analyzed PbS QDPDs using ultrafast transient absorption (TA) spectroscopy after exciting the PbS QDs with a 190 fs pulse at 1200 nm; see Supporting Information S3 for details. As a first reference,

https://doi.org/10.1021/acs.nanolett.6c01775
Nano Lett. 2026, 26, 8315−8322

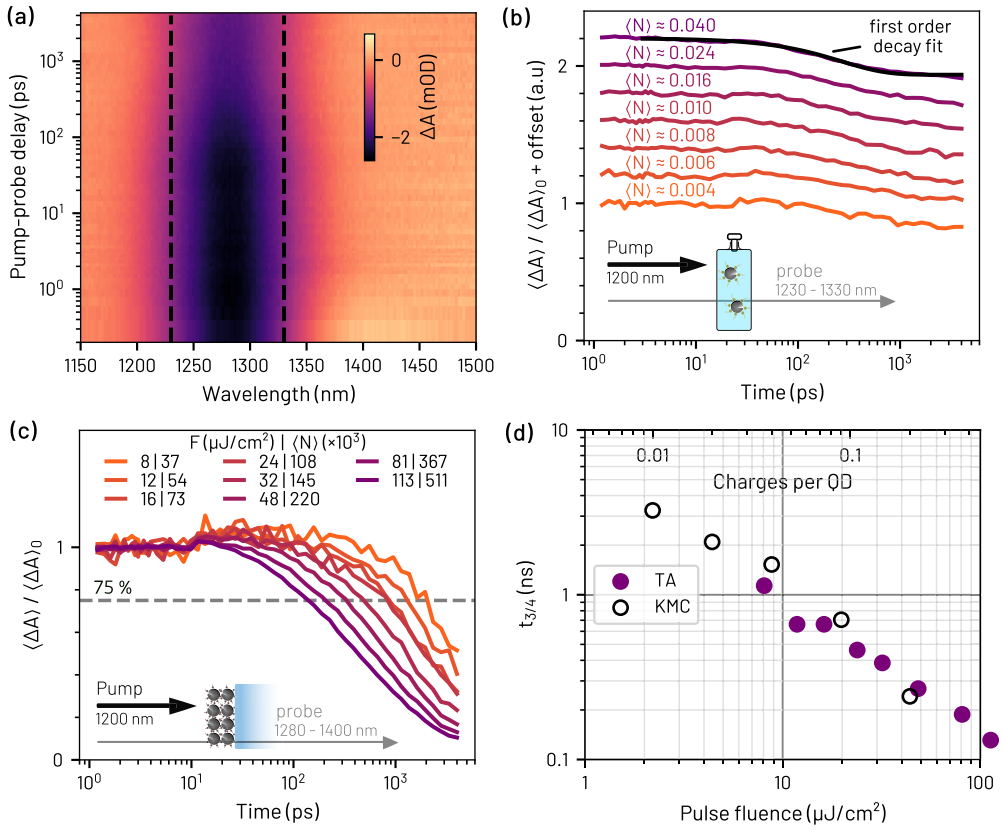

Figure 2. Analysis of recombination dynamics in 4.6 nm PbS QDs (1300 nm band gap) under varying conditions using a 1200 nm pump and band-edge probe. (a) Example 2D false color TA map, here in solution phase. The black dashed lines indicate the spectral averaging window for the time traces in (b). (b) Normalized time traces of $\Delta A(t)$ as a measure for $n(t)$, for different initial excitation densities $\langle N \rangle$ in the solution phase. We observe no dependence of the charge recombination on the initial excitation density in this regime, and all traces can be reproduced by a first order decay fit with a lifetime of 145 ps. A visual offset is added to the graphs for better visibility. (c) Normalized time traces for the same QDs as (a, b) in film after ligand exchange, now showing a much faster decay at increasing $\langle N \rangle$, albeit still in a regime far below unity. Note that here no offset is added to the graphs to emphasize the accelerating decay under increasing fluence. (d) Quarter-decay time of the traces in panel c show an increase in decay rate. Experimental data (TA, filled markers) is compared with kinetic Monte Carlo (KMC) simulations (empty markers).

Figure 2a displays a wavelength/delay time map of the differential absorbance $\Delta A(\lambda, t)$ recorded on PbS-1300 QDs with as-synthesized ligands in solution, for a pump level creating $\langle N \rangle \approx 0.08$. We assign the narrow, negative ΔA band centered around 1280 nm to the bleach of the $1S_h - 1S_e$ band-edge transition.[28] To mitigate the impact of spectral shifts, we analyze in what follows the average bleach between 1230 nm and 1350 nm as a function of the pump−probe delay.[29]

Figure 2b represents the decay of this average bleach for different pump fluences, where each trace was normalized to the initial bleach. Apart from the constant offset added for clarity, one sees that the resulting traces are identical, irrespective of the initial exciton number. This result indicates that any relaxation process is first order in $\langle N \rangle$ and thus related to single electron−hole pairs. For quantification, we fitted the bleach decay to the sum of a first-order decay and a constant bleach. We found that the decay affects about 20% of the initial bleach and is characterized by a rate constant $k_1 = 6.9\ \text{ns}^{-1}$, equivalent to a lifetime of 145 ps; see Supporting Information S4. Given the above discussion, we assigned this partial loss of the band-edge bleach to trapping of single charge-carriers by surface defects in about 1 out of 5 PbS-1300 QDs. Using higher pump fluences, we determined the biexciton Auger lifetime of PbS-1300 at 21 ps in Supporting Information S4, in line with the literature.[30] For PbS-950, a similar analysis yielded a single-exciton trapping time of 73 ps and a biexciton Auger lifetime of 8 ps.

As outlined in Supporting Information S5, TA spectroscopy on films of as-synthesized PbS-1300 and PbS-950 yielded similar power-independent normalized bleach decays. After TBAI exchange, however, PbS-1300 films exhibit a markedly power-dependent bleach recovery. As shown in Figure 2c, the normalized bleach in such a device-ready film disappears more quickly for a higher initial carrier density, even when $\langle N \rangle \ll 1$. Also in the PbS-950 films after EDT exchange that are p-type, the decay is very similar; see Supporting Information S5. Moreover, for both films, a mere 10% of the initial bleach remains at longer delay times at the highest exciton densities. This result suggests that in device-ready films, most, if not all, charge carriers are affected by fast recombination processes. As shown in Figure 2c, we characterized the underlying decay process through the quarter-delay time $t_{3/4}$, which is the pump−probe delay at which the relative bleach has dropped to 75% of the initial bleach. Note that we prefer $t_{3/4}$ over, for example, a half-delay time $t_{1/2}$, since a 25% charge-carrier loss is also reached at a low excitation powers, given the 4 ns time range of our experiments.

Figure 2d indicates that $t_{3/4}$ is approximately proportional to the inverse of the pulse energy, which is expected for a loss process that is second-order in $\langle N \rangle$ and affects all charge carriers. Still, this result may rather describe the net effect of a

https://doi.org/10.1021/acs.nanolett.6c01775
Nano Lett. 2026, 26, 8315−8322

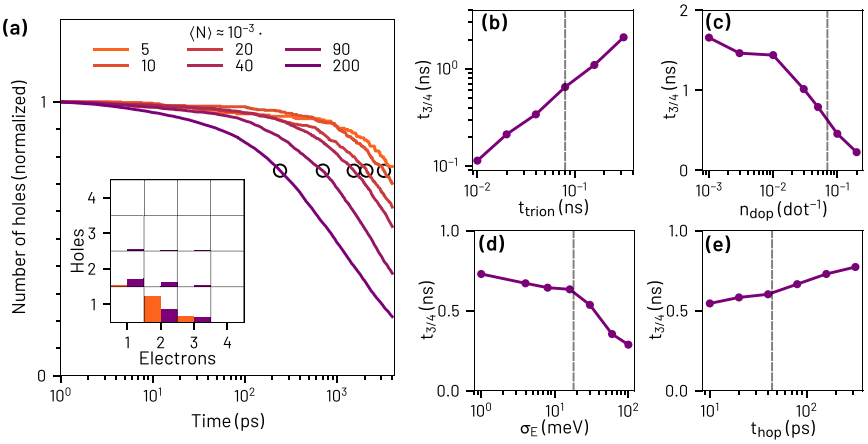

Figure 3. Kinetic Monte Carlo simulations. (a) The time evolution of the hole density for increasing photoexcitation density $\langle N \rangle$ from 0.005 to 0.2. The background doping density is 0.07 charges per QD. The inset shows the charge complexes responsible for recombination, where the height of the block represents the relative amount of recombination events due to the specific (n, p) combination - with n electrons and p holes per QD. A negative trion for example corresponds to (2, 1). Data are shown for 0.005 (orange) and 0.2 (purple) excitations per QD. (b−e) Influence of different simulation parameters on the quarter-decay time. Only one parameter is changed at a time, while the others are pinned iteratively to a trion decay rate t_{trion} = 80 ps, doping density n_{dop} = 0.07, σ_E = 18 meV, and t_{hop} = 44 ps. The dashed line indicates the default parameter for each case.

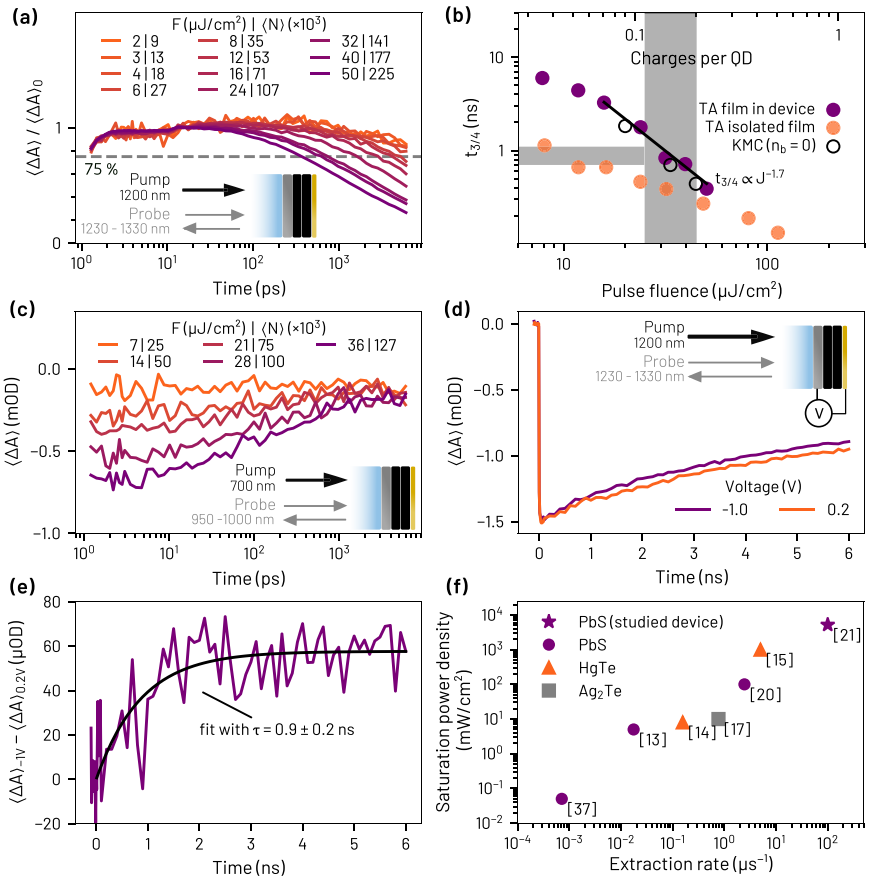

Figure 4. (a) Bleach decay traces of the small band gap QDs embedded in a full device stack under open circuit conditions. (b) Quarter-decay time as a function of excitation density shows that the accelerating decay persist in devices. The horizontal shaded area illustrates the experimental estimate of the drift time. The vertical shaded area is bounded by the lowest and highest measured saturation fluences for various devices. (c) Bleach decay traces of the large band gap QDs (same device) show a fast decay in the hole transport layer. (d) The effect of reverse bias on the bleach decay at a fixed excitation of 6.8 $\mu J/cm^2$, below device saturation. The small voltage dependency suggests charge separation without carrier extraction. (e) The difference between the bleach decay at +0.2 V and −1 V shows a transient that is characteristic for the transport of charges through the device, obtaining a transport time of 0.9 ± 0.2 ns from a single exponential fit. (f) Literature overview of the highest reported continuous-wave optical power within the linear dynamic range (LDR), as a function of the charge extraction rate; see references in brackets.

https://doi.org/10.1021/acs.nanolett.6c01775
Nano Lett. 2026, 26, 8315−8322

more involved recombination process. For example, even for an average occupation $\langle N \rangle \ll 1$, hopping of mobile charge carriers in a QD film can lead to the temporary formation of trions, for which Auger recombination results in the rapid loss of an electron−hole pair. Furthermore, the probability of trion formation can be larger than expected since TBAI ligand exchange turns the PbS QD film *n*-type, thereby creating a background density of electrons.[6] Assigning charge-carrier loss to Auger recombination of trions, and taking a background electron density into account, the charge-carrier loss rate can be expressed as

$$\frac{dn}{dt} = -k_3 n_T = -\frac{k_3}{n_{QD}^2}(n + n_b)^2 p \quad (1)$$

$$= -\frac{k_3}{n_{QD}^2}(n_b^2 n + 2n_b n^2 + n^3) \quad (2)$$

Here, n_T is the density of trions in the QD film, k_3 the rate constant for trion recombination, n and p the density of photogenerated electrons and holes, and n_b the doping-induced background density of electrons. We rewrote n_T as the product of the total electron density, and the probability $(n + n_b)p/n_{QD}^2$ that a given QD holds an additional electron/hole pair. Assuming $n = p$ for optical excitation, eq 2 indicates that trion-induced electron−hole recombination is a mixed-order process that shifts from first-order in the photogenerated charge density at low ($n \ll n_b$) to third-order at high carrier density ($n \gg n_b$).

To better describe the loss of electron−hole pairs through Auger recombination, we implemented a kinetic Monte Carlo (KMC) approach to simulate the interplay between formation, recombination, and separation of multicharge states in a QD film. As detailed in Supporting Information S6, we arranged QDs in a simple cubic lattice, described charge-carrier hopping through the Marcus model with a hopping rate in agreement with the experimentally measured mobility, and allowed for Auger recombination of trions and higher-order multicarrier states.[31] Figure 3a represents the decay of $\langle N \rangle$—normalized to the initial exciton number—obtained through KMC simulation where we took a background doping of 0.07 charges per QD (6×10^{17} cm^{-3}),[32] while reference values for other parameters were taken as listed in Supporting Information S6. All simulation parameters originate from the literature or experimental considerations, except the background doping density. In agreement with the bleach decay, the simulated $t_{3/4}$ shortens with increasing exciton number and approximates the observed reciprocal relation to the pulse energy; see Figure 2d. The inset of Figure 3a depicts the relative occurrence of the different multicarrier states involved in Auger recombination. In agreement with the above discussion, negative trions are indeed the dominant state at low excitation density ($\langle N \rangle = 0.005$). At $\langle N \rangle = 0.2$, on the other hand, other multi-carrier states, such as positive trions and biexcitons, increasingly contribute to charge carrier losses through Auger recombination.[24]

In Figure 3b−e, we illustrate how different simulation parameters affect $t_{3/4}$, where dashed lines always represent the reference setting, and the initial exciton number was taken as $\langle N \rangle = 0.1$. As could be expected, $t_{3/4}$ increases almost proportionally with the trion recombination time. Regarding the majority carrier density, the quarter-decay time is approximately constant when photogenerated charge carriers dominate but shortens considerably when the background density increases. Energy disorder only has an effect when exceeding kT, and also the hopping time has little impact on $t_{3/4}$ within the range of hopping rates considered. Note that these simulations are not PbS specific. Any QD film will exhibit similar loss curves when the underlying process parameters are comparable.[33] Finally, note that an alternative explanation for the accelerated decay rate is given by trap assisted Auger recombination. In Supporting Information S6, we found that this requires a trap density around 0.5 per QD, which is unlikely given the high EQE of our devices at low optical density.

Figure 4a−e summarizes the results of a spectroscopic analysis of an entire QDPD stack, where the differential absorbance was measured by pumping at 1200 nm and capturing the reflected probe pulse using either 1230−1330 nm or 950−1000 nm white light. Figure 4a shows the normalized bleach decay of PbS-1300 recorded on the QDPD under open circuit conditions. Similar to the device-ready film, we observed a progressive acceleration of the bleach decay when increasing the initial charge density. However, the quarter-decay times obtained from this bleach decay are significantly longer than in the stand-alone film; see Figure 4b. Referring to eq 1, such a slower loss rate of photogenerated charge carriers can reflect a lower background charge density, a likely result when the built-in field within the QDPD stack depletes the QD film.[12] As shown in Figure 4b, the experimentally obtained quarter-decay time is in good agreement with the KMC simulations when the background doping is eliminated, as expected in the fully depleted film. We thus conclude that, also in the QDPD device stack, Auger recombination of multicarrier states increases the charge-carrier loss rate at higher charge densities, even in the $\langle N \rangle \ll 1$ limit.

In Figure 4c, we present complementary measurements, where we probed the band-edge bleach of PbS-950 after excitation using 700 nm pumping. In this case, quarter-decay times drop below 100 ps even at the low exciton numbers used in this experiment. Referring to the bleach decay shown in Figure S8 of Supporting Information S5, this decay is faster than that of the device-ready films, a clear contrast with PbS-1300. As can be seen from the stack design shown in Figure 1a, the PbS-950 layer is in direct contact with the gold electrode. Possibly, this creates an additional charge-recombination pathway or causes an increased background density of holes in the PbS-950 film that accelerates charge carrier loss. Either way, we conclude that the charges photogenerated in the PbS-1300 film can be more effectively extracted from the QDPD than charges formed in the PbS-950 film.

In Figure 4d, we plot the bleach decay recorded on the QDPD using identical excitation conditions—creating on average 0.035 excitons per QD—but applying an electrical bias of either −1 or 0.2 V. Referring to Figure 1b, the photocurrent is nearly bias-independent at −1 V, while 0.2 V is close to the zero-current bias. As can be seen in Figure 4b, the $\langle N \rangle = 0.035$ excitation level yields a quarter-decay time of several ns under open-circuit conditions. Even so, Figure 4e shows that the bleach decay recorded under both biases is not identical but diverges with a characteristic time constant of 0.9 ns. With increasing reverse bias, the drift time of photogenerated charge-carriers to cross the QD film will shorten. In a 50 nm thick QD film under a bias of −1 V, charge carriers with a mobility of 2.5×10^{-2} cm^2/V·s will have a drift time of 1

https://doi.org/10.1021/acs.nanolett.6c01775
Nano Lett. 2026, 26, 8315−8322

ns. We therefore assign the divergence between both bleach traces to the faster charge carrier separation under a −1 V reverse bias. As a result, the continued decay of the bleach at a longer delay time may reflect the transfer of photogenerated charges from the QD film to the electron and hole transport layer. In that case, both the extraction and loss of charge carriers contribute to the bleach decay, with the latter becoming dominant in the faster decay traces recorded at the higher exciton numbers.

Building on the above discussion, it follows that the extracted fraction of the charge carriers photogenerated within the PbS-1300 layer hinges on the balance between charge carrier separation and charge-carrier loss. Under conditions where charge-carrier loss is slower than separation, a fixed fraction of the photogenerated charges—possibly 100%—will be extracted, and the EQE will be independent of the illumination power. On the other hand, the extracted fraction will drop when the charge-carrier loss rate increases, which will eventually reduce the EQE. Following this description, a measure of the saturation fluence $J_{3/4}$ is the fluence at which the quarter-decay time $t_{3/4}$ and the drift time of the charge carriers match. Considering the variation of $t_{3/4}$ with pump fluence shown in Figure 4b, this is precisely what we found. Fluences in the range 25−45 μJ/cm^2 yield a $t_{3/4}$ in the range 0.7−1.1 ns, in agreement with the estimated drift time over the stack of 0.9 ns.

The relation between $t_{3/4}$ and $J_{3/4}$ provided through the fluence-dependent decay of the normalized bleach applies to photocurrent saturation under pulsed illumination. In the literature, however, saturation characteristics are typically recorded using CW illumination. In that case, the QDPD attains a steady state in which the charge generation rate G equals the sum of the charge-carrier loss and extraction rate. As discussed in Supporting Information S7, relating photocurrent saturation to the power density Φ_{sat} where the nonlinear loss rate matches the linear extraction rate, we have

$$\Phi_{sat} \approx \frac{n_{sat}}{\tau_d}\frac{2\epsilon_{ph}}{\sigma} \tag{3}$$

Here, σ is the QD absorption cross section, ϵ_{ph} is the photon energy, n_{sat} is the steady-state carrier density at saturation, and τ_d is the dwell time of charge-carrier in the active layer.

Interestingly, the relevant parameters of the individual QDs—absorption coefficient and Auger-recombination rate—are rather independent of the material, and the relevant QD size effects partly cancel out each other (see Supporting Information S7).[34−36] Therefore, eq 3 describes a unique relation between the saturation power and the charge-carrier extraction time. For devices that are not RC-limited, τ_d can be estimated from the fall time of the QDPD response. As outlined in Supporting Information S7, we obtained the extraction time from literature studies that both report the temporal response and the saturation behavior of the QDPDs analyzed. These studies make use of different QDs—including PbS, HgTe, and Ag_2Te—and exhibit a wide range of saturation powers.[37] Nevertheless, Figure 4f shows a common, approximately reciprocal relation between Φ_{sat} and τ_{ext} for all these QDPDs. According to estimates provided in Supporting Information S7, this saturation curve corresponds to a carrier density of 10^{-3} to 10^{-2}, a result confirming that QDPDs show saturation well below the $\langle N\rangle \approx 1$ level. On the other hand, we conclude from Figure 4f that the linear dynamic range of QDPDs can be extended by extracting photogenerated charge carriers faster from the QD film. This is achieved by increasing the mobility of the QD film or lowering the device thickness at the expense of reduced absorption. Another possibility is using a higher reverse bias voltage, but this might also increase the dark current and does not necessarily extend the linear dynamic range.

In summary, we investigated photocurrent saturation in state-of-the-art PbS quantum dot photodiodes (QDPDs) by means of femtosecond transient absorption spectroscopy. As compared to as-synthesized, isolated QDs, we show that device-ready QD films and operating QDPDs are characterized by a specific charge carrier loss mechanism that accelerates with increasing charge-carrier densities, even if the average exciton number $\langle N\rangle$ remains well below 1. By means of Monte Carlo simulations, we assign this critical additional loss pathway to substantial multiexciton Auger recombination in films with mobile charge carriers, i.e., trion-type recombination. Furthermore, we show that photocurrent saturation in QDPDs occurs at incident power densities where the loss rate of the photogenerated charge carriers matches the charge-carrier drift time across the QD film. Based on this quantitative insight, we show that published saturation power densities systematically increase for QDPDs with shorter charge carrier extraction times, and we conclude that extending the linear dynamic range requires mainly a faster extraction of photogenerated charge carriers from the QD film.

■ ASSOCIATED CONTENT

Supporting Information

The Supporting Information is available free of charge at https://pubs.acs.org/doi/10.1021/acs.nanolett.6c01775.

Details on device fabrication, characterization of the device EQE, calculation of the absorption cross section in the solution phase and in solid films, details on the transient absorption spectroscopy, TA analysis of single and biexcitons in the PbS QDs in the solution phase, further analysis of the same PbS QDs in the solid phase, details on the kinetic Monte Carlo simulations and further simulations results, derivation of the relation between dwell time and saturation fluence and a literature comparison of different material systems (PDF)

■ AUTHOR INFORMATION

Corresponding Authors

Pieter Geiregat − *Physics and Chemistry of Nanostructures, Department of Chemistry, Ghent University, 9000 Gent, Belgium; NOLIMITS Core Facility for Non-Linear Microscopy and Spectroscopy, Ghent University, 9000 Gent, Belgium;* orcid.org/0000-0001-7217-8738; Email: Pieter.Geiregat@UGent.be

Zeger Hens − *Physics and Chemistry of Nanostructures, Department of Chemistry, Ghent University, 9000 Gent, Belgium;* orcid.org/0000-0002-7041-3375; Email: Zeger.Hens@UGent.be

Authors

Korneel Molkens − *Physics and Chemistry of Nanostructures, Department of Chemistry, Ghent University, 9000 Gent, Belgium; Photonics Research Group, Department of Information Technology and NOLIMITS Core Facility for*

https://doi.org/10.1021/acs.nanolett.6c01775
Nano Lett. 2026, 26, 8315−8322

Non-Linear Microscopy and Spectroscopy, Ghent University, 9000 Gent, Belgium

Yu-Hao Deng − *Physics and Chemistry of Nanostructures, Department of Chemistry, Ghent University, 9000 Gent, Belgium;* orcid.org/0000-0002-8828-3820

Ezat Kheradmand − *Physics and Chemistry of Nanostructures, Department of Chemistry, Ghent University, 9000 Gent, Belgium*

Dries Van Thourhout − *Photonics Research Group, Department of Information Technology, Ghent University, 9000 Gent, Belgium;* orcid.org/0000-0003-0111-431X

Complete contact information is available at: https://pubs.acs.org/10.1021/acs.nanolett.6c01775

Notes

The authors declare no competing financial interest.

■ ACKNOWLEDGMENTS

D.V.T., P.G., and Z.H acknowledge support from FWO Vlaanderen through the FWO-SBO program AVALON (S000626N) and research project nos. G037221N, G0B2921N, and S0002019N. P.G. and D.V.T. acknowledge support from the European Commission (H2020-ERC STG NOMISS, Grant Agreement No. 101077526 and ERC AdG 884963). P.G. and Z.H. acknowledge Ghent University for research funding (IBOF-COFLIGHT 25/076, BOF-GOA 01G02124).

■ REFERENCES

(1) Houtepen, A. J.; Sargent, E. H.; Infante, I.; Owen, J. S.; Green, P. B.; Schaller, R. D.; Bals, S.; Zeiske, S.; Stöferle, T.; Hens, Z. Colloidal Quantum Dots for Optoelectronics. *Nature Reviews Methods Primers* **2025**, *5*, 42.

(2) Wang, Y.; Wu, H.; Rodà, C.; Peng, L.; Taghipour, N.; Dosil, M.; Konstantatos, G. Shortwave Infrared Light Detection and Ranging Using Silver Telluride Quantum Dots. *Adv. Mater.* **2025**, *37*, No. 2500977.

(3) Allen, M.; Malik, S.; Bower, C.; Liu, Y.; Kallioinen, S.; Nenonen, M.; So, D.; Colli, A.; Tamminen, J.; Routama, J.; Haque, S.; Coenen, F.; Hämäläinen, J.; Andrew, P.; Ryhänen, T. In *Infrared Technology and Applications L*; SPIE, 2024; Vol. *13046*, pp 91−100.

(4) Fang, F.; Tang, Y.; Tang, H.; Song, Y.; Chen, Q.; Rao, L.; Xiao, S.; Chen, W.; Cao, L. Interface-Enhanced PbS Quantum Dot Short-Wave Infrared Photodetector toward Instant Smoke Detection Applications. *ACS Applied Electronic Materials* **2025**, *7*, 7368−7376.

(5) Hendricks, M. P.; Campos, M. P.; Cleveland, G. T.; Jen-La Plante, I.; Owen, J. S. A Tunable Library of Substituted Thiourea Precursors to Metal Sulfide Nanocrystals. *Science* **2015**, *348*, 1226−1230.

(6) Brown, P. R.; Kim, D.; Lunt, R. R.; Zhao, N.; Bawendi, M. G.; Grossman, J. C.; Bulović, V. Energy Level Modification in Lead Sulfide Quantum Dot Thin Films through Ligand Exchange. *ACS Nano* **2014**, *8*, 5863−5872.

(7) Vafaie, M.; Fan, J. Z.; Morteza Najarian, A.; Ouellette, O.; Sagar, L. K.; Bertens, K.; Sun, B.; García de Arquer, F. P.; Sargent, E. H. Colloidal Quantum Dot Photodetectors with 10-Ns Response Time and 80% Quantum Efficiency at 1,550 Nm. *Matter* **2021**, *4*, 1042−1053.

(8) Kim, D.; Si, M.-J.; Kim, J.; Jung, Y.; Baek, S.-W. Recent Advances in Colloidal Quantum Dots-Based Shortwave Infrared Photodetectors. *Adv. Opt. Mater.* **2026**, *14*, No. e02859.

(9) Dong, C.; Liu, S.; Barange, N.; Lee, J.; Pardue, T.; Yi, X.; Yin, S.; So, F. Long-Wavelength Lead Sulfide Quantum Dots Sensing up to 2600 Nm for Short-Wavelength Infrared Photodetectors. *ACS Appl. Mater. Interfaces* **2019**, *11*, 44451−44457.

(10) Wang, H.; Pinna, J.; Romero, D. G.; Di Mario, L.; Koushki, R. M.; Kot, M.; Portale, G.; Loi, M. A. PbS Quantum Dots Ink with Months-Long Shelf-Lifetime Enabling Scalable and Efficient Short-Wavelength Infrared Photodetectors. *Adv. Mater.* **2024**, *36*, No. 2311526.

(11) Xu, Q.; Meng, L.; Sinha, K.; Chowdhury, F. I.; Hu, J.; Wang, X. Ultrafast Colloidal Quantum Dot Infrared Photodiode. *ACS Photonics* **2020**, *7*, 1297−1303.

(12) Deng, Y.-H.; Pang, C.; Kheradmand, E.; Leemans, J.; Bai, J.; Minjauw, M.; Liu, J.; Molkens, K.; Beeckman, J.; Detavernier, C.; Geiregat, P.; Van Thourhout, D.; Hens, Z. Short-Wave Infrared Colloidal QD Photodetector with Nanosecond Response Times Enabled by Ultrathin Absorber Layers. *Adv. Mater.* **2024**, *36*, No. 2402002.

(13) Georgitzikis, E.; Malinowski, P. E.; Li, Y.; Maes, J.; Hagelsieb, L. M.; Guerrieri, S.; Hens, Z.; Heremans, P.; Cheyns, D. Integration of PbS Quantum Dot Photodiodes on Silicon for NIR Imaging. *IEEE Sensors Journal* **2020**, *20*, 6841−6848.

(14) Yang, J.; et al. Ligand-Engineered HgTe Colloidal Quantum Dot Solids for Infrared Photodetectors. *Nano Lett.* **2022**, *22*, 3465−3472.

(15) Gréboval, C.; et al. HgTe Nanocrystal-Based Photodiode for Extended Short-Wave Infrared Sensing with Optimized Electron Extraction and Injection. *ACS Applied Nano Materials* **2022**, *5*, 8602−8611.

(16) Leemans, J.; Pejović, V.; Georgitzikis, E.; Minjauw, M.; Siddik, A. B.; Deng, Y.-H.; Kuang, Y.; Roelkens, G.; Detavernier, C.; Lieberman, I.; Malinowski, P. E.; Cheyns, D.; Hens, Z. Colloidal III−V Quantum Dot Photodiodes for Short-Wave Infrared Photodetection. *Adv. Sci.* **2022**, *9*, No. 2200844.

(17) Wang, Y.; Peng, L.; Schreier, J.; Bi, Y.; Black, A.; Malla, A.; Goossens, S.; Konstantatos, G. Silver Telluride Colloidal Quantum Dot Infrared Photodetectors and Image Sensors. *Nat. Photonics* **2024**, *18*, 236−242.

(18) Peng, L.; Wang, Y.; Ren, Y.; Wang, Z.; Cao, P.; Konstantatos, G. InSb/InP Core−Shell Colloidal Quantum Dots for Sensitive and Fast Short-Wave Infrared Photodetectors. *ACS Nano* **2024**, *18*, 5113−5121.

(19) Siddik, A. B.; Song, W.; Georgitzikis, E.; Vildanova, M.; Jin, M.; Berghmans, F.; Lieberman, I.; Malinowski, P. E.; Conard, T.; Cheyns, D.; Heremans, P. InAs Colloidal Quantum Dot Photodiode Stack for CMOS-Integrated Infrared Imaging. *ACS Nano* **2025**, *19*, 32780.

(20) Tran, H.-C. V.; Jang, E.; Kim, J.; Choi, M.; Park, Y.; Jeong, H.; Goo, T.; Bae, S.; Jeong, S. Enhanced SWIR Photodetection in Colloidal Quantum Dot Photodiodes via Tunneling Current Suppression. *ACS Appl. Mater. Interfaces* **2025**, *17*, 15666−15674.

(21) Pang, C.; Deng, Y.-H.; Kheradmand, E.; Poonkottil, N.; Petit, R.; Elsinger, L.; Detavernier, C.; Geiregat, P.; Hens, Z.; Van Thourhout, D. Integrated PbS Colloidal Quantum Dot Photodiodes on Silicon Nitride Waveguides. *ACS Photonics* **2023**, *10*, 4215−4224.

(22) Pecunia, V.; et al. Guidelines for Accurate Evaluation of Photodetectors Based on Emerging Semiconductor Technologies. *Nat. Photonics* **2025**, *19*, 1178−1188.

(23) Justo, Y.; Geiregat, P.; van Hoecke, K.; Vanhaecke, F.; De Mello Donega, C.; Hens, Z. Optical Properties of PbS/CdS Core/Shell Quantum Dots. *J. Phys. Chem. C* **2013**, *117*, 20171−20177.

(24) Gao, Y.; Sandeep, C. S. S.; Schins, J. M.; Houtepen, A. J.; Siebbeles, L. D. A. Disorder Strongly Enhances Auger Recombination in Conductive Quantum-Dot Solids. *Nat. Commun.* **2013**, *4*, 2329.

(25) Gilmore, R. H.; Lee, E. M. Y.; Weidman, M. C.; Willard, A. P.; Tisdale, W. A. Charge Carrier Hopping Dynamics in Homogeneously Broadened PbS Quantum Dot Solids. *Nano Lett.* **2017**, *17*, 893−901.

(26) Deng, Y.-H.; Kheradmand, E.; Pang, C.; Siddik, A. B.; Bai, J.; Lieberman, I.; Geiregat, P.; Van Thourhout, D.; Hens, Z. Super Bending-Stable Flexible Colloidal QD Photodetector with Fast Response and Near-Unity Carrier Extraction Efficiency. *ACS Appl. Mater. Interfaces* **2025**, *17*, 14243−14249.

(27) Vest, R. E.; Grantham, S. Response of a Silicon Photodiode to Pulsed Radiation. *Appl. Opt.* **2003**, *42* (25), 5054−5063.

(28) Gesuele, F.; Sfeir, M. Y.; Koh, W.-K.; Murray, C. B.; Heinz, T. F.; Wong, C. W. Ultrafast Supercontinuum Spectroscopy of Carrier Multiplication and Biexcitonic Effects in Excited States of PbS Quantum Dots. *Nano Lett.* **2012**, *12*, 2658−2664.
(29) Geiregat, P.; Houtepen, A.; Justo, Y.; Grozema, F. C.; Van Thourhout, D.; Hens, Z. Coulomb Shifts upon Exciton Addition to Photoexcited PbS Colloidal Quantum Dots. *J. Phys. Chem. C* **2014**, *118*, 22284−22290.
(30) Stewart, J. T.; Padilha, L. A.; Qazilbash, M. M.; Pietryga, J. M.; Midgett, A. G.; Luther, J. M.; Beard, M. C.; Nozik, A. J.; Klimov, V. I. Comparison of Carrier Multiplication Yields in PbS and PbSe Nanocrystals: The Role of Competing Energy-Loss Processes. *Nano Lett.* **2012**, *12*, 622−628.
(31) Yazdani, N.; Andermatt, S.; Yarema, M.; Farto, V.; Bani-Hashemian, M. H.; Volk, S.; Lin, W. M. M.; Yarema, O.; Luisier, M.; Wood, V. Charge Transport in Semiconductors Assembled from Nanocrystal Quantum Dots. *Nat. Commun.* **2020**, *11*, 2852.
(32) Wang, R.; Shang, Y.; Kanjanaboos, P.; Zhou, W.; Ning, Z.; Sargent, E. H. Colloidal Quantum Dot Ligand Engineering for High Performance Solar Cells. *Energy Environ. Sci.* **2016**, *9*, 1130−1143.
(33) Lhuillier, E.; Chen, M.; Lan, X.; Sahu, A.; Jeong, K. S.; Reiss, P.; Jeong, S.; Rogach, A. L. What the Inheritance of IV−VI and II−VI Semiconductors Teaches Us for the Quest of Heavy Metal-Free Nanocrystals Dedicated to Infrared Detection. *Nano Lett.* **2026**, *26*, 4923.
(34) Schaller, R. D.; Pietryga, J. M.; Klimov, V. I. Carrier Multiplication in InAs Nanocrystal Quantum Dots with an Onset Defined by the Energy Conservation Limit. *Nano Lett.* **2007**, *7*, 3469−3476.
(35) Geiregat, P.; Houtepen, A. J.; Sagar, L. K.; Infante, I.; Zapata, F.; Grigel, V.; Allan, G.; Delerue, C.; Van Thourhout, D.; Hens, Z. Continuous-Wave Infrared Optical Gain and Amplified Spontaneous Emission at Ultralow Threshold by Colloidal HgTe Quantum Dots. *Nat. Mater.* **2018**, *17*, 35−42.
(36) Melnychuk, C.; Guyot-Sionnest, P. Slow Auger Relaxation in HgTe Colloidal Quantum Dots. The. *J. Phys. Chem. Lett.* **2018**, *9*, 2208−2211.
(37) Nikitskiy, I.; Goossens, S.; Kufer, D.; Lasanta, T.; Navickaite, G.; Koppens, F. H. L.; Konstantatos, G. Integrating an Electrically Active Colloidal Quantum Dot Photodiode with a Graphene Phototransistor. *Nat. Commun.* **2016**, *7*, No. 11954.

https://doi.org/10.1021/acs.nanolett.6c01775
Nano Lett. 2026, 26, 8315−8322